JOURNAL OF SPACECRAFT AND ROCKETS
Vol. 43, No. 6, November–December 2006

Far-Field Spectral Analysis of a Space Shuttle Vernier Reaction Control System Firing

Lawrence S. Bernstein* and Matthew Braunstein†
Spectral Sciences, Inc., Burlington, Massachusetts 01803
A. Lyle Broadfoot‡
University of Arizona, Tucson, Arizona 85721
William L. Dimpfl§,††
Aerospace Corporation, Los Angeles, California 90009-2957
and
Rainer A. Dressler,‖,†† Yu-hui Chiu,¶,†† James A. Gardner,¶ and Edmond Murad**
U.S. Air Force Research Laboratory, Space Vehicles Directorate, Hanscom Air Force Base, Massachusetts 01731

DOI: 10.2514/1.21252

Near-UV OH(A–X) and NH(A–X) emission bands at ∼3100 and 3360 Å, respectively, have been observed in the far-field radiance from the shuttle vernier reaction control system engine exhaust using the GLO imager spectrograph located in the payload bay during the STS-74 mission. Spectra were collected at a resolution of 4 Å for daytime solar illumination conditions during low-Earth-orbit maneuvers. A temporal analysis (2 s temporal resolution) of spectral features is presented for an extended vernier reaction control system burn. The spectrum is dominated by the narrow NH(A–X) band. Both NH(A–X) and OH(A–X) features are shown to be proportional to the engine mass flow, and thus are produced by a single collision or solar-induced mechanism. Whereas a pure chemical mechanism, yet unknown, has been established for the NH(A–X) feature, the weaker OH(A–X) band is demonstrated to be primarily produced by the chemical reaction of atmospheric O with exhaust H_2O, with minor solar-induced contributions. The high signal-to-noise ratio for both bands allowed a more precise determination of excited state rovibrational populations compared with previous efforts. The present analysis is complemented with direct simulation Monte Carlo calculations of the engine-exhaust flow field and proposed radiation excitation mechanisms for the NH(A–X) and OH(A–X) emissions.

Nomenclature

E	=	energy
E_a	=	activation energy
$E_{\max}$	=	energy cut off, above which quantum state populations are ignored
$F(t)$	=	time dependent thrust level
I	=	emission intensity (photons s^{-1} cm^{-2})
I_o	=	thrust-to-intensity conversion constant (photons s^{-2} cm^{-2} N^{-1})
k	=	reaction rate coefficient
k_B	=	Boltzmann constant
$NH(A^3\Pi)$	=	first triplet excited state of NH
$NH(X^3\Sigma^-)$	=	NH ground electronic state
[O]	=	O atom density
$OH(A^2\Sigma^+)$	=	OH first excited electronic state
$OH(X^2\Pi)$	=	OH ground electronic state
$O(^3P)$	=	atomic oxygen ground state
P	=	NH(A–X) precursor
P'	=	oxygenated reaction product of NH(A–X) chemiluminescent source reaction
T	=	temperature
T_r	=	rotational temperature
t, t'	=	time
t_1	=	collision time constant
u	=	relative velocity
v'	=	vibrational quantum number of the upper electronic state
v''	=	vibrational quantum number of the lower electronic state
W	=	rotational state weighting factor
χ_P	=	mole fraction of NH(A–X) precursor P
ρ	=	gas number density
σ	=	reaction cross section
σ_{el}	=	elastic scattering cross section
σ_{ram}	=	emission cross section observed at ram angle of attack

Received 21 November 2005; accepted for publication 22 February 2006.

*Chief Scientist, Spectral Sciences, Inc., 4 Fourth Avenue.
†Group Leader, Computational Physics and Chemistry, Spectral Sciences, Inc.
‡Senior Research Scientist, Lunar and Planetary Laboratory.
§Senior Research Scientist, Aerospace Corporation, PO Box 92957- M2/266.
‖Task Scientist, U.S. Air Force Research Laboratory.
¶Staff Scientist, U.S. Air Force Research Laboratory.
**Retired, Emeritus.
††Member AIAA.

Introduction

WHEN low-Earth orbiting spacecraft fire an engine, the far-field collisional interaction between engine-exhaust molecules and thermospheric constituents, primarily atomic oxygen O and molecular nitrogen, can produce substantial spatially-integrated emissions which typically exceed that of the near-field vacuum core emissions by orders of magnitude. Because the exhaust molecular velocity (∼3.5 km/s) with respect to the spacecraft velocity (∼7.7 km/s) is high, the intensity and spectral characteristics of the radiance depend strongly on the thrust axis angle of attack. In a ram firing (retrograde burn), the relative velocity of interaction of ∼11 km/s results in center-of-mass collision energies in the range of ∼5–7 eV for collisions of O with exhaust

species. This "extra" translational energy enables potential reaction channels to exceed their activation energies and thus significantly increase the number of possible chemiluminescent processes. During the 1990s, a suite of imagers and spectrographs called GLO was successfully flown on five different missions in the space shuttle bay [1,2]. The GLO spectrograph covered an unprecedented spectral range, 1150–9000 Å, at resolutions ranging from ~4 Å (UV) to ~10 Å (IR). The first measurements revealed two prominent near-UV features that were attributed to $OH(A^2\Sigma^+\text{-}X^2\Pi)$ and $NH(A^3\Pi\text{-}X^3\Sigma^-)$ emissions at 3086 and 3360 Å, respectively, when the primary reaction control system (PRCS) engine was fired into the ram direction in darkness [3]. Hereafter, we refer to these emissions as OH(A–X) and NH(A–X) emissions. Similar observations were subsequently made from the space station Mir [4,5]. The fact that the emissions were more prominent at distances beyond 10 m instead of immediately after the nozzle led to the conclusion that the bands arise from luminescence produced by the molecular collisions between engine-exhaust species and the thermospheric constituents.

A recent detailed analysis [6] of GLO spectral measurements of PRCS burns during both sunlit and night-sky conditions resulted in the conclusion that the OH(A–X) emissions arise from three distinct mechanisms

$$O(^3P) + H_2O \rightarrow OH(A^2\Sigma^+) + OH(X^2\Pi) \quad \Delta H = -4.79 \text{ eV} \tag{1}$$

$$H_2O + h\nu \rightarrow OH(A) + H \tag{2}$$

$$OH + h\nu \rightarrow OH(A) \tag{3}$$

where reaction (1) signifies a far-field chemiluminescent reaction between exhaust H_2O, cooled in the supersonic expansion, and thermospheric O; reaction (2) is photodissociation of exhaust H_2O by Lyman-α and other vacuum ultraviolet spectral lines; and reaction (3) describes photoexcitation of trace amounts of cold hydroxyl radical in the exhaust. Depending on the type of engine, the OH mole fraction may reach values as high as 4×10^{-3} [7–9]. Because the energy disposed in $OH(A)$ is significantly different in processes 1–3, the observed OH(A–X) spectrum will depend significantly on lighting conditions, thrust angle of attack, and thermospheric properties.

The threshold energy for reaction (1) greatly exceeds the chemical energy available from the kinetic energy of the oxygen atoms alone (~0.1 eV). This channel is opened only when the exhaust jet of the engine is directed into the atmospheric wind (i.e., a ram firing), where the exhaust H_2O and orbital velocities provide additional translational energy to the collision system. This is confirmed by the failure to observe OH(A–X) emissions at an angle of attack of 90 deg at night viewing conditions. From their analysis, Bernstein et al. [6] estimated an emission cross section associated with reaction (1) of 1.7×10^{-18} cm^2 at ram conditions.

The $NH(A)$ emissions are attributed to a single collision reaction of an engine-exhaust precursor P with atmospheric atomic oxygen O

$$O(^3P) + P \rightarrow NH(A) + P'O \tag{4}$$

The identity of P is not well established, with the leading candidates from earlier analysis being potential trace exhaust constituents CH_2NH, HNCO, HCN, and HNC [3]. There is no significant solar-driven component to the $NH(A)$ emissions, as nearly the same signal level is observed for night and day firings of the same engine under comparable conditions (i.e., firing geometry and atmospheric density). The precursor candidates resulted from selecting all species that conformed to the reaction thermochemistry, defined by the apparent activation energy for the reaction, and the guidelines for usual bimolecular chemistry. Among these, HCN could be tested in the laboratory [10] and was found to not produce observable NH(A–X) radiance at pertinent collision energies. A difficulty with the remaining candidates is their low stability, which makes it hard to justify concentrations high enough to produce the observed intensity. More recently, following analysis of CO(a) Cameron band plume emission [11], NH_3, which is stable, has been added to the list of candidates. The Cameron band analysis indicated minor amounts (~1% mole fraction) of CH_4 in plumes of methyl substituted amine propellant engines. NH_3 is the nitrogen analogue to CH_4 and, therefore, can also be expected to be present in plumes of amine propellant engines in similar minor amounts. To satisfy the thermochemistry requirement, however, the reaction

$$O(^3P) + NH_3 \rightarrow NH(A) + H_2O - 2.98 \text{ eV} \tag{5}$$

must be invoked. Because two hydrogen atoms are transferred in reaction (5), a short-range process associated with a small cross section is expected. This work provides an opportunity to place better bounds on the multiplicative product of the precursor mole fraction and the cross sections. Under the assumption that P is a single species, and independent of engine, the comparison between 870 pounds of force (lbf) thrust PRCS and 25 lbf thrust vernier reaction control system (VRCS) NH(A–X) radiance intensities shows that the mole fraction of P is significantly higher for the latter [3]. This is quite plausible, as one expects the exhaust composition of the VRCS engine to be much further from equilibrium (i.e., kinetically controlled) than the much larger PRCS engine, thus favoring a much higher mole fraction of the precursor.

In the present work, we present the analysis of an additional set of GLO near-UV spectra recorded on STS-74 during an extended daytime firing of a Shuttle VRCS engine that lasted approximately 35 s. The present measurements were taken at a significantly lower altitude of 344.5 km compared with the ~390 km measurements during the STS-63 mission described in [6]. Because of the higher thermospheric densities, the far-field radiance was significantly more intense, resulting in improved signal-to-noise that allowed an analysis of the smaller VRCS engine in more detail including a temporal analysis of the extended firing sequence. The OH(A–X) and NH(A–X) intensities and spatial distributions were also modeled using the direct simulation Monte Carlo (DSMC) code, SOCRATES [12].

The higher quality OH(A–X) spectrum for the VRCS engine also allowed resolution of a puzzling aspect of the previous analysis of the STS-63 spectrum for a PRCS engine [6]. In the earlier work, the OH (A–X) spectrum indicated a potentially significant contribution from the $OH(A)$ $v' = 3$ and 4 vibrational levels. These levels are highly predissociated and are normally not observed [13–16]. The new results do not show evidence of these bands, thus the previous results are now attributed to noise from the much lower quality PRCS spectrum.

Space Conditions and Instrument

The data presented in this work were acquired from the GLO-IV spectrometer aboard the STS-74 space shuttle mission which occurred between 12–20 November 1995. The orbital velocity is 7.7×10^3 m s^{-1}. Assuming corotation of the thermosphere, the spacecraft velocity with respect to the atmosphere averaged $\sim 7.4 \times 10^3$ m s^{-1} in the mission's west–east orbit at an inclination of 51.6 deg. The spectral data were acquired during a series of ram firings of the 25 lbf thrust R5R VRCS engine that uses N_2O_4-monomethylhydrazine fuel. The analysis focuses on a 140 s time period on 18 November, during which the R5R engine was fired repeatedly, and in some instances continuously, for ~35 s. The detailed time history of the engine operation of interest in this work is presented in Fig. 1. Although somewhat difficult to resolve in this plot, the regions of intermittent thrust correspond to 50% duty cycle pulsed engine operation with 1 s on/off cycles. The exhaust product mole fractions of the major species based on nonequilibrium calculations [9] are 0.34 (H_2O), 0.31 (N_2), 0.17 (H_2), 0.14 (CO), and 0.04 (CO_2). An axial exhaust velocity of 3.5×10^3 m s^{-1} was assumed, which originates from the exit velocity of 3×10^3 m s^{-1} plus an additional 0.5×10^3 m s^{-1} attained in the vacuum expansion [8,9]. Thus, the overall plume-atmosphere collision velocity along

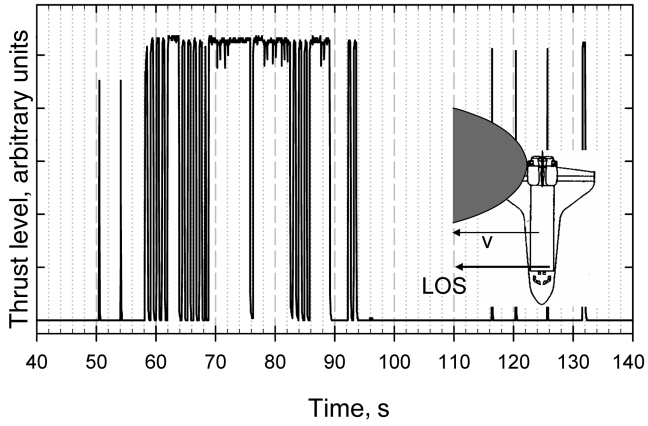

Fig. 1 R5R VRCS firing sequence and measurement geometry for the GLO sensor.

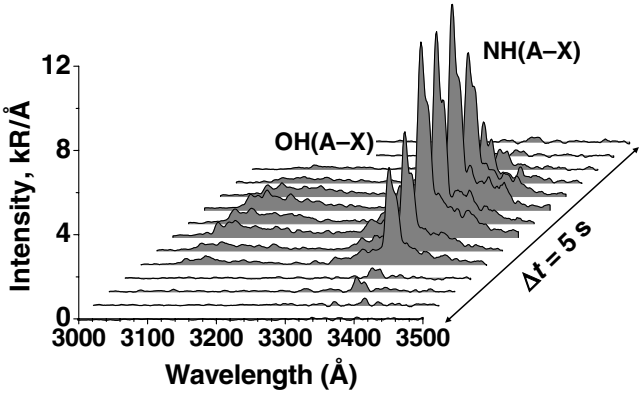

Fig. 2 GLO near-UV spectral measurements of firing sequence in Fig. 1.

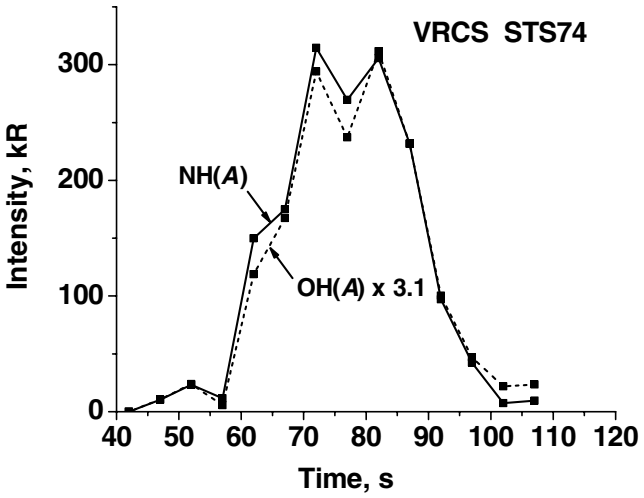

Fig. 3 Temporal profiles of absolute NH(A–X) and OH(A–X) band intensities.

the thrust axis is $\sim 10.9 \times 10^3$ m s^{-1}, providing more than sufficient energy to enable a host of plume-atmosphere reactions giving rise to optical emissions. The firing occurred on 18 Nov. 1995 at an altitude of 344.5 km, at a latitude of −11.5 deg, and a longitude of −33.3 deg. The universal time is 17.92 h corresponding to a local time of 15.7 h. Based on the mass spectrometer and incoherent scatter (MSIS) data model [16–18], the thermospheric temperature was 870 K and the atomic oxygen density was 1.8×10^8 cm^{-3}. The GLO line-of-sight (LOS) is also shown in Fig. 1 and takes on an azimuthal angle parallel to the thrust axis which is also parallel to the indicated velocity vector in a ram firing. The LOS also had an elevation angle of 15 deg. At this viewing geometry, the LOS intersects the exhaust gases at a distance of >50 m from the nozzle exit, thereby avoiding emissions from the hot near-field area of the exhaust while observing substantial column densities of the exhaust-atmosphere interaction region. Also, the viewing geometry is such that the exhaust species remain in the field-of-view for times comparable to the period between collisions with thermospheric constituents (see later discussion).

The space-borne GLO instrument has been described in detail previously [1,2]. It was mounted in the front section of the shuttle bay during the STS-74 mission. It comprises a nine-section spectrograph, three monochromatic imagers, and a TV camera, all boresighted to view in the same direction. The spectrograph and imagers have intensified CCD (ICCD) focal-plane detectors. The nine slightly overlapping spectrograph sections permit simultaneous recording of the spectrum from 115.0 to 900.0 nm with a spectral resolution of about 4–10 Å. Their combined focal-plane image is 4500 pixels wide in the wavelength (dispersion) dimension, perpendicular to the slit, and 192 pixels in the spatial dimension, along the slit. The slit image at the detector is a narrow portion of the image of the distant object being observed, preserving spatial resolution in the slit-length direction. The design of the slit and foreoptics affords a field-of-view of 0.2×8.5 deg.

The instrument head was mounted on a scan platform that permitted viewing in almost any direction. A TV-camera image was used while in flight to select the view direction, track the day or night earth limb, and hold stars steady in the spectrograph slit for spectral calibrations and occultation experiments. A computer was dedicated to carrying out preprogrammed, complex experiment sequences that are time-tagged, and/or ground-commanded. The instrument was therefore autonomous and capable of continuous operation throughout a 14-day mission. Science and engineering data were returned on communications links via the tracking and data relay satellites (TDRS) at a total data-return rate of 1.5 Mbits/s. Data acquisition and downloading are described in separate publications [3,19]. The laboratory spectral sensitivity calibration procedure of the detector, as well as the spectral calibration approach, has been described previously [2]. The sensitivity calibration of the space-based measurements was crossed-checked using standard star observations. Although this significantly increases the confidence level of absolute radiance measurements, it is difficult to quantify the wavelength dependent accuracy.

Space-Based Spectral Measurements

A sequence of near-UV spectra in the 3000–3500 Å spectral region for the series of VRCS firings shown in Fig. 1 is displayed in Fig. 2. The spectra were collected at 5 s intervals with 2 s averaging. Two spectral features centered at 3100 and 3360 Å become apparent following the onset of the burn during the acquisition period of the fourth spectrum. The weak signals near 3360 Å which precede the main burn sequence are attributed to the two brief engine firings at ~50 and 54 s (see Fig. 1). The two main features have been previously observed [3] and are attributed to OH(A–X) and NH(A–X) emissions, respectively. Unlike the far-field radiance observed during PRCS day and night-sky firings [6], the NH(A–X) band in the present VRCS daytime observation is significantly more intense than the OH(A–X) feature, suggesting that the precursor P in reaction (4) is either different or more abundant. No differences in spectral features are observed for both bands within signal-to-noise limits.

The temporal histories of OH(A–X) and NH(A–X) total intensities, obtained through spectral integration of the bands shown in Fig. 2, are presented in Fig. 3. The intensities are obtained from integration of the spectral bands shown in Fig. 2. The actual measurement times are indicated by the squares. The accuracy of the absolute radiances is estimated at ±10 kR based on the integrated noise following the burn sequence. The OH(A) curve is scaled by a factor of 3.1 to facilitate comparison to the NH(A) curve. The nearly identical temporal profiles of both band intensities indicate that they both arise from chemical pathways involving the same number of reaction steps. A previous analysis of the OH(A–X) spectra suggested single-step mechanisms involving either solar-induced or chemical reaction pathways [reactions (1–3)] [6].

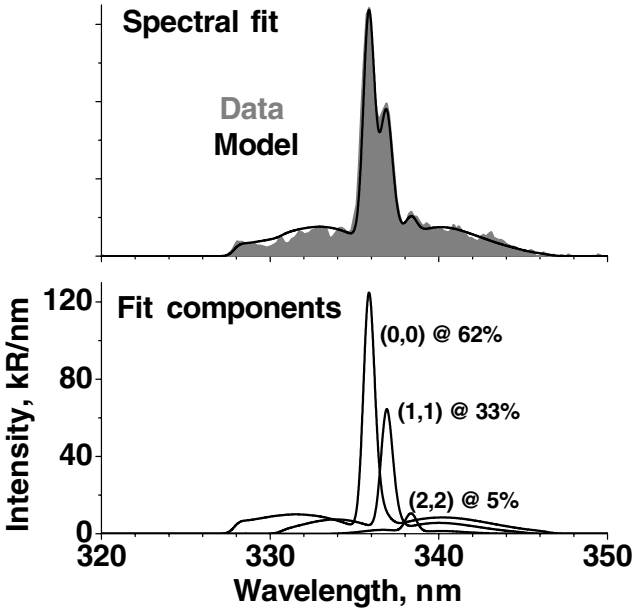

Fig. 4 Spectral fit to averaged most intense NH(A–X) spectra.

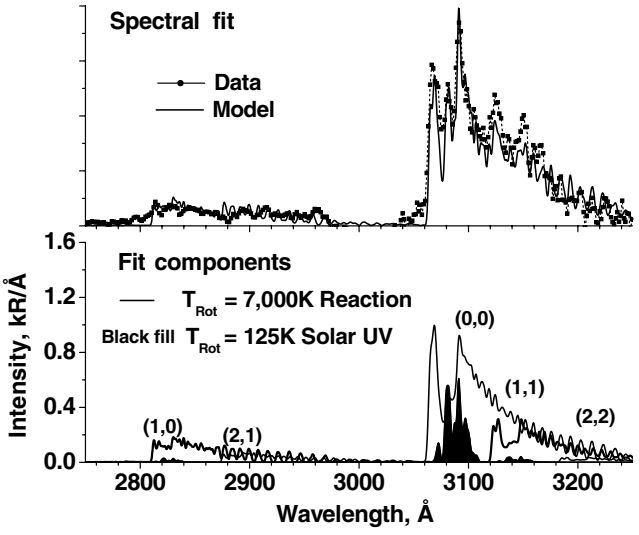

Fig. 5 Spectral fit to averaged most intense OH(A–X) spectra.

Data Analysis

The OH(A–X) and NH(A–X) emission spectra are highly nonequilibrium (i.e., not simply described in terms of a single temperature). The methods and code used to fit these spectra have been previously described by Dimpfl et al. [20] In addition, we have used the program, Diatomic, to simulate the observed spectra [21]. Both methods produce essentially identical results, the latter having the added convenience of a Windows interface. The results are shown in Figs. 4 and 5 for the NH(A–X) and OH(A–X) bands, respectively, and the fit parameters are given in Table 1. The top panel in Fig. 4 compares the observed NH(A–X) spectrum, consisting of a summed average of the most intense spectral frames during the firing sequence, to a model calculation. Spectral fits to individual frames show no significant change in the resulting analysis. The bottom panel shows the individual calculated vibrational band components of the modeled spectrum. The spectrum can be reproduced with $\Delta v = 0$ bands for A-state vibrational levels $v' = 0, 1, 2$. The upper state rotational temperatures providing the best fit are 5500, 3000, and 1000 K for the (0,0), (1,1), and (2,2) bands, respectively. The derived vibrational and rotational energy distributions are nearly identical to those reported previously for a PRCS ram burn, implying an identical precursor [3].

The time-averaged OH(A–X) band shown in Fig. 5, top panel, exhibits very good signal-to-noise despite its lower peak intensity. The spectral features are noticeably dissimilar with the daytime PRCS spectra reported in [6]. Those spectra were recorded during the STS-63 mission at a higher altitude of 390 km. The significantly lower thermospheric O densities resulted in a spectrum that was predominantly attributed to solar-induced processes. At the lower altitude and higher O density of the present STS-74 burn, it can be expected that the daytime spectra have significantly higher contributions from the chemical reaction mechanism (1). This is corroborated by the present model analysis shown in the bottom panel of Fig. 5. The spectral fits were constrained such that the maximum allowed vibration–rotation energy for a given OH(A) state was less than the predissociation threshold $E_{\max} = 1.5$ eV. The primary contribution of the OH(A–X) (0–0) band is associated with a high rotational temperature of 7000 K. This is consistent with the analysis of a PRCS night-sky ram-burn spectrum [6] of the same STS-63 mission, where a lower rotational temperature of 4000 K was determined at conditions where light-induced processes were negligible. That measurement, however, had significantly lower signal-to-noise due to the lower thermospheric densities. Consequently, the current analysis is regarded to be more representative of the reaction-driven emission spectrum. In particular, we note that the VRCS spectrum does not display any contribution from the OH(A) $v' = 3$ and 4 states which are highly predissociated, and only a small contribution from $v' = 2$ is deduced from the spectral fit, consistent with the moderate degree of predissociation for this level.

Even though the VRCS observation was made during the day, the contribution of the solar UV-driven pathways (reactions (2) and (3)) is minor. Only the cold vacuum core OH component is positively identified and it accounts for ~10% or 10 kR of the spectrally integrated observed intensity at peak intensity of 104 kR of the temporal profile. This is consistent with previously described model calculations [6] of the solar components, which for the VRCS engine and observation geometry (GLO sensor at front end of the payload bay) predicts 7.3 kR for the OH solar-excited emission and 0.5 kR for the photo-dissociated H_2O channel. It was shown in the previous analysis of the PRCS OH(A) spectra that the vibrational temperature of the solar-excited OH(A) is dependent on the absorption optical opacity of the cold OH(X). In that case, a vibrational temperature of 5000 K was determined, corresponding to high absorption opacity. However, the VRCS engine is much smaller and corresponds to optically thin conditions and is characterized by an OH(A) vibrational temperature of 2200 K. The solar-driven components scale in direct proportion to column density/vehicle thrust, whereas the reactive pathway for OH(A) is limited by the atmospheric O flux, which increases with decreasing altitude. Thus, there will be a thrust-dependent altitude below which the reactive mechanism overtakes the solar UV mechanism.

As shown recently in an analysis of the UV CO Cameron emission observed from various firings of the shuttle OMS and PRCS engines [20], the number of chemical steps involved in a particular emission can be inferred from the startup or shutdown transients of the engine firing. It was found that a simple, approximate chemical kinetic approach yielded results (i.e., the temporal intensity profile) comparable to more accurate and detailed DSMC-based calculations. For an arbitrary engine firing sequence, the intensity (both the LOS and total spatial emission) for a one-step mechanism can be approximated by

$$I(t') = I_o \int_0^{t'} dt F(t) \exp[-(t' - t)/t_1] \tag{6}$$

The collision time constant is estimated from

$$t_1 = \frac{1}{\rho \sigma_{\text{el}} u} \tag{7}$$

We evaluated Eq. (7) for the VRCS firing sequence of Fig. 1 using $\rho = 2.0 \times 10^8$ cm^{-3}, $\sigma_{\text{el}} = 1.0 \times 10^{-15}$ cm^2 (estimated for

Table 1 Parameters providing the best reproduction of the OH(A–X) and NH(A–X) spectral bands.

Component	$P\nu'(\nu' = 0, 1, 2)$	T_r, K	E_{max}(cm^{-1})
NH(A–X)			
O + P	0.62, 0.33, 0.05	5500, 3000, 1000	
OH(A–X)			
Exhaust OH	$T_{\nu'} = 2200$ K	125	12,000
O + H_2O	0.61, 0.32, 0.07	7000	12,000

the O-NH precursor collisions), and $u = 10.9 \times 10^5$ cm/ s^{-1}. This results in $t_1 = 4.6$ s, which is considerably longer than the approximately 1 μs radiative lifetime of NH(A) and, therefore, represents an effective rise or decay time of the observed near-UV radiance for engine startup or shutdown. A two-step mechanism would imply a collision time that is at least twice as long, and would greatly alter the temporal profile as discussed in the preceding sections [11]. The comparison of the predicted temporal emission profile to that observed for the NH(A–X) band is depicted in Fig. 6. The width of the squares correspond to the measurement times. For simplicity, a slightly temporally-averaged representation of the actual firing sequence (see Fig. 1) was employed. A 2 s boxcar average was applied to the model profile to simulate the GLO sensor temporal integration. As shown in Fig. 3, the OH(A–X) temporal profile is virtually identical. The overall agreement, particularly the slopes of the startup and shutdown transients, is good and further confirms that both the VRCS NH(A–X) and OH(A–X) emissions are formed by one-step reactions.

Predictions of the NH(A–X) and OH(A–X) emission intensities were performed using the DSMC code, SOCRATES [12]. It uses standard DSMC methods that have been tuned to efficiently capture chemistry and radiation processes. The DSMC Cartesian spatial grid extended from -300 to $+100$ m in the x direction and -400 to $+400$ m in the y and z directions, with the atmospheric wind pointing toward the $+x$ direction and the engine flux pointing in the $-x$ direction (ram geometry). There were 20 spatial cells in the x direction and 32 spatial cells in each of the y and z directions with cell dimensions varying from 15 m near the engine source to about 36 m near the edges of the grid. The DSMC move time was 4.0×10^{-4} s, and $\sim$15, 000 steady-state samples were obtained after steady state was reached at about $\sim$1000 move steps. Approximately 500,000 simulated particles were contained in the grid during a single move time. A standard variable hard sphere [22] scattering model was used with $\omega = 0.75$ for all collision partners.

The velocity-dependent cross sections for the single-step chemistries used in the calculations are displayed in Fig. 7. The relative distribution of collision velocities about the mean ram collision velocity of 10.9 km/s^{-1} and the local atmospheric

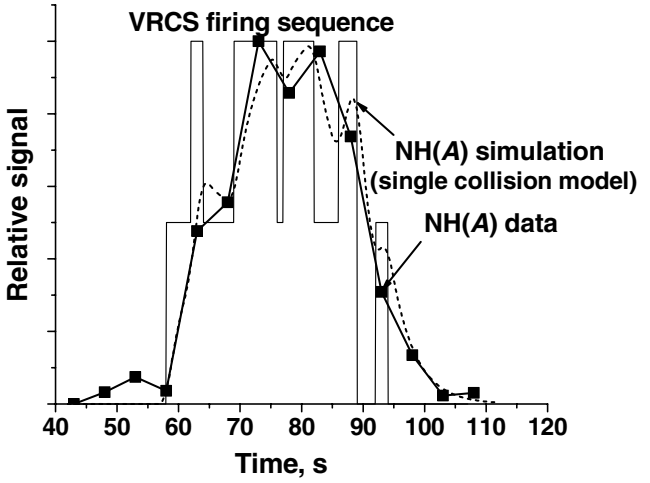

Fig. 6 Comparison of observed and modeled temporal intensity profile for NH(A–X) emissions.

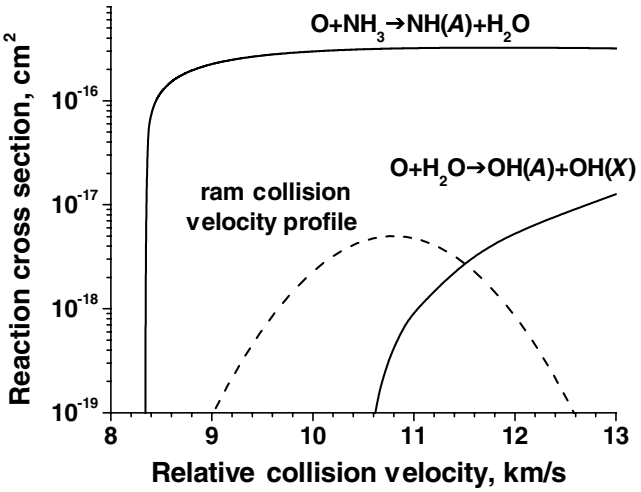

Fig. 7 Velocity-dependent cross sections for the NH(A) and OH(A) reaction pathways.

temperature of 870 K is also shown. The OH(A–X) chemiluminescent emission cross sections were deduced from the PRCS night ram burn that was discussed in preceding sections

$$\sigma(E) = A(E\text{-}E_a)^n/E, \qquad E \geq E_a$$
$$A = 1.4 \times 10^{-17}\ \text{cm}^2\,\text{eV}^{-0.8},$$
$$E_a = 4.79\ \text{eV}, \qquad n = 1.8 \tag{8}$$

and correspond to the temperature dependent rate coefficient (cm^3 s^{-1}) [6]

$$k = 7.4 \times 10^{-17} T^{1.3} \exp(-E_a/k_B T) \tag{9}$$

This rate coefficient is about 20% lower than that derived in the original work because we have since retrieved through the MSIS model a $\sim$20% higher atomic oxygen density at the time of the respective experiment [16–18].

The chemistry turns on steeply near the ram-firing collision velocity of 10.9 km/s^{-1}. Figure 7 also shows the distribution of collision velocities, which is broad due to the thermal spread in O atom velocities given by the 870 K thermospheric temperature. The broad distribution plays an important part in enhancing the effective reaction cross section, providing access to the much larger higher-velocity portion of the cross section curve. We note that in the preceding analysis of the PRCS data it was suggested that the total OH(A)-state excitation cross section could be considerably larger because a significant fraction of OH(A) may be formed in states that predissociate [6]. The current analysis demonstrates that the predissociating states do not contribute noticeably to the observed spectrum. However, because of the high predissociation branching ratios [11,13–15], this does not preclude their formation in the O + $H_2O \rightarrow$ OH(A) + OH(X) reaction. Thus, the reaction cross section derived in this work should be viewed as the total photon production cross section, as opposed to the total reaction cross section, which may be considerably larger.

In case of the NH(A–X) emissions, the evidence points clearly to a source consisting of a 1-step chemical reaction, most likely involving thermospheric O and an unknown precursor P [reaction (4)]. In the preceding analysis of the radiance from a PRCS ram firing, it was assumed that every incident atomic oxygen undergoes a collision with an exhaust molecule [6]. This is corroborated by ground-based observations that show that essentially no radiance is observed in a significant volume between the spacecraft and the region of peak intensity [3]. The present SOCRATES calculations, discussed next, show that this assumption also holds for the smaller VRCS engine. Consequently, the presently observed peak intensities with line-of-sight close to the thrust axis allow the derivation of the product of precursor mole fraction and cross section at ram conditions

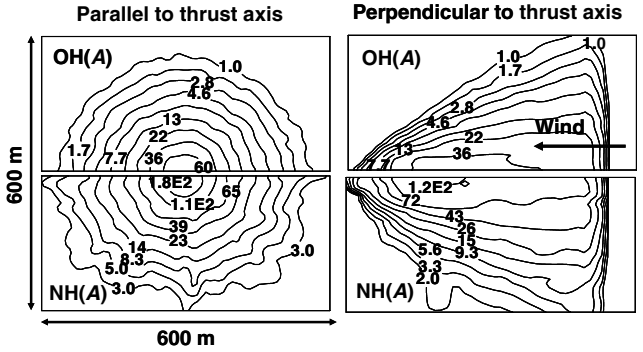

Fig. 8 SOCRATES calculations of spatial intensity contours for the NH(A–X) and OH(A–X) bands.

$$\sigma_{\text{ram}}\chi_P = \sigma_{\text{el}}\frac{I}{[\text{O}]u} \tag{10}$$

From the observed peak radiance of 323 kR, a cross section–mole fraction product of 1.6×10^{-18} cm^2 is derived for a nominal relative velocity, $u = 10.9 \times 10^5$ cm/s^{-1}. To model the radiance, an estimated exhaust mole fraction of 0.005 for the proposed precursor NH_3 is chosen to be consistent with the ~0.01 mole fraction of CH_4 required for the CO(a) emission (as discussed in the introduction) [20]. This implies an excitation cross section of $\sigma_{\text{ram}} = 3.2 \times 10^{-16}$ cm^2. The respective rate coefficient for $O + NH_3 \rightarrow NH(A) + H_2O$ is set at

$$k = 5.4 \times 10^{-10}\exp(-E_a/k_BT) \tag{11}$$

where we assume an activation energy provided by the thermochemical threshold of 2.98 eV (68.5 kcal/mole) [23]. The value of the preexponential factor was determined by constraining the velocity-dependent cross section corresponding to Eq. (10) to equal the data-derived value for the ram firing. Equation (11) corresponds to a cross section energy dependence of (cm^2, energy units eV)

$$\sigma(E) = 1.12 \times 10^{-15}(E - E_a)^{0.5}/E \tag{12}$$

The DSMC calculations of the ram-firing VRCS engine NH(A–X) and OH(A–X) radiance using the SOCRATES code [12] are shown in Fig. 8 for both the onboard observation geometry (left panel) and for a remote observer with line-of-sight perpendicular to the thrust axis. The contours are spaced logarithmically in units of kR. Because of the cylindrical symmetry of the ram plume, only the top or bottom half plane of the spatial imagery for each view and emitter is displayed. The "irregularities" in the contours are not real plume features and are a consequence of the slow convergence of the DSMC-based solution method. The left panels are for a sensor looking parallel to the VRCS thrust axis located in a plane which runs through the shuttle bay and is perpendicular to the thrust axis. This corresponds closely to the GLO observation geometry. For this view, the shuttle location is coincident with the peak contour value (not displayed). The right panels are for an off-board sensor looking broadside to the plume. For this view, the shuttle is located at the left edge where the panels meet. The sharp boundary at ~550 m is a result of using a finite solution region and corresponds to the outer boundary of the solution region. Note that for this view, the intensity peaks ~150 m [48 and 165 kR for OH(A) and NH(A)] ahead of the shuttle because the incoming atmospheric O flux cannot penetrate the exhaust flow all the way to the shuttle. The OH(A–X) prediction of ~94 kR on the axis of the onboard view agrees well with the observed value of 94 kR which has been corrected for the ~10 kR contribution of the solar-excited OH vacuum core component. We estimate the accuracy of the calculated radiance to be approximately 40% based on grid density variations. The presently reported values are based on the highest grid density used.

The good agreement between calculated and observed intensities demonstrates that the cross section derived in the preceding section applies satisfactorily to a much lower-altitude, higher-density, and lower thrust observation. The broadside observations show that there is a significant area between the shuttle and the peak intensity where no radiance is observed. This confirms that all incident O atoms in vicinity of the thrust axis undergo a collision with an exhaust molecule, and that Eq. (10) applies. This is further corroborated by the fact that the SOCRATES NH(A–X) prediction of 314 kR on the axis of the onboard view also agrees well with the observed value of 323 kR used to derive the product between mole fraction and emission cross section applied in the calculation. The suggested NH (A–X) emission cross section can, therefore, also be applied to other engines to determine the relative mole fraction of P in comparison with the present VRCS engine. In case of the earlier work on a PRCS ram burn [6], the NH(A–X) emission was observed in a similar axial viewing geometry. From the observed integrated radiance, we determine that the precursor mole fraction is a factor of 7 lower than in the VRCS engine.

Conclusions

A detailed, temporal, and spectral analysis of an extended VRCS engine burn is presented. The present analysis supports and refines previous retrievals of spectral parameters and reaction cross sections for NH(A–X) and OH(A–X). The temporal evolution of the NH(A–X) and OH(A–X) emissions are consistent with a single-step reaction of a plume species with atmospheric O. In the OH(A–X) case, the spectrum is highly altitude dependent due to the varying relative contributions of solar-induced and chemical reaction mechanisms. We recommend an NH(A–X) formation rate constant of $5.4 \times 10^{-10}\exp(-2.98\ \text{eV}/k_BT)$ cm^3/s^{-1} based on a precursor exhaust mole fraction of 0.005. The space-based data discussed in this work can be obtained by contacting the corresponding author, Rainer A. Dressler.

Acknowledgments

The authors thank Donald E. Hunton (AFRL/VSBXT) for several vital corrections and comments. This work has been initiated and partially funded by the U.S. Air Force Office of Scientific Research under tasks 2301HS 02VS06 (program manager, Kent Miller). L. S. Bernstein and M. Braunstein of Spectral Sciences, Inc., acknowledge support from the U.S. Air Force Research Laboratory under contract F19628-00-C-0006 (program manager, R. A. Dressler). W. L. Dimpfl of Aerospace Corporations acknowledges support from the U.S. Space and Missile Systems Center and the U.S. Air Force Research Laboratory. The authors also gratefully acknowledge support from the U.S. Air Force Office of Scientific Research under task 2303ES02 (program manager, Michael R. Berman).

References

[1] Viereck, R. A., Knecht, D. J., Broadfoot, A. L., and Sandel, B., "The AIS: A Spectrograph/Imager Ensemble for Space Flight," Air Force Geophysics Lab., Rept. GL-TR-90-0158, May 1990.

[2] Broadfoot, A. L., Sandel, B. R., Knecht, D., Viereck, R., and Murad, E., "A Panchromatic Spectrograph with Supporting Monochromatic Imagers," *Applied Optics*, Vol. 31, No. 6, 1992, pp. 3083–3096.

[3] Viereck, R. A., Murad, E., Knecht, D. J., Pike, C. P., Bernstein, L. S., Elgin, J. B., and Broadfoot, A. L., "The Interaction of the Atmosphere with the Space Shuttle Thruster Plume: the NH(A–X) 336 nm Emission," *Journal of Geophysical Research*, Vol. 101, No. A3, 1996, pp. 5371–5380.

[4] Karabadzhak, G. F., Pastinin, Y., Khmelinin, B., Teslenko, V., Shvets, N., Drakes, J. A., Swann, D. A., and McGregor, W. K., "Experimentation Using the Mir Station as a Space Laboratory," AIAA Paper 98-0288, Jan. 1998.

[5] Karabadzhak, G. F., Pastinin, Y., Afanasiev, A., Szhenov, E., Drakes, J. A., McGregor, W. K., Bradley, D., Teslenko, V., Shvets, N., Volkov, O., and Kukushkin, V., "Measurements of the Progress-M Main Engine Retrofiring Plume at Orbital Conditions," AIAA Paper 99-1042, Jan. 1999.

[6] Bernstein, L. S., Chiu, Y., Gardner, J. A., Broadfoot, A. L., Lester, M. I., Tsiouris, M., Dressler, R. A., and Murad, E., "Molecular Beams in Space: Sources of OH(A–X) Emission in the Space Shuttle Environment," *Journal of Physical Chemistry A*, Vol. 107, No. 49, 2003, pp. 10695–10705.

[7] Pickett, J. S., Murphy, G. B., and Kurth, W. S., "Gaseous Environment of the Shuttle Early in the Spacelab 2 Mission," *Journal of Spacecraft and Rockets*, Vol. 25, No. 2, 1988, pp. 169–174.

[8] Pickett, J. S., Murphy, G. R., Kurth, W. S., Goertz, C. K., and Shawhan, S. D., "Effects of Chemical Releases by the STS-3 Orbiter on the Ionosphere," *Journal of Geophysical Research*, Vol. 90, No. A4, 1985, pp. 3487–3497.

[9] Viereck, R. A., Bernstein, L. S., Mende, L. S., Murad, S. B., and Swenson, E., "Visible Spectra of Thruster Plumes from the Space Shuttle Primary Reaction Control System," *Journal of Spacecraft and Rockets*, Vol. 30, No. 6, 1993, pp. 724–730.

[10] Orient, O. J., Chutjian, A., Martus, K. E., and Murad, E., "Observation of CN A $\rightarrow$ X and B $\rightarrow$ X Emissions in Gas-Phase Collisions of Fast O (^3P) atoms with HCN.," *Physical Review A*, Vol. 48, No. 1, 1993, pp. 427–431.

[11] Dimpfl, W. L., Light, G. C., and Bernstein, L. S., "Molecular Dynamics from Remote Observation of CO(a) from Space Shuttle Plumes," *Journal of Spacecraft and Rockets*, Vol. 42, No. 2, 2005, pp. 352–362.

[12] Braunstein, M., and Cline, J. A., "Progress on Parallelizing a General Purpose Direct Simulation Monte Carlo (DSMC) Code for High Performance Computing Applications," *U.S. Air Force Maui Optical and Supercomputing Site Tech Conference*, Maui Economic Development Board, Maui, HI, 2003, pp. 1–10.

[13] Copeland, R. A., Jeffries, J. B., and Crosley, D. R., "The $OHA^2\Sigma^+$-$X^2\Pi_i$ (4, 2) Band: Line Positions and Line Widths," *Journal of Molecular Spectroscopy*, Vol. 143, No. 1, 1990, pp. 183–185.

[14] Parlant, G., and Yarkony, D. R., "A Theoretical Analysis of the State-Specific Decomposition of OH($A^2\Sigma^+$, v', N', F_1/F_2) Levels, Including the Effects of Spin-Orbit and Coriolis Interaction," *Journal of Chemical Physics*, Vol. 110, No. 1, 1999, pp. 363–376.

[15] Spaanjaars, J. J. L., ter Meulen, J. J., and Meijer, G., "Relative Predissociation Rates of OH A $v' = 3$ from Combined Cavity Ring-Down/Laser-Induced Fluorescence Measurements," *Journal of Chemical Physics*, Vol. 107, No. 7, 1997, pp. 2242–2248.

[16] Yarkony, D. R., "A Theoretical Treatment of the Predissociation of the Individual Rovibronic Levels of OH/OD($A^2\Sigma^+$)," *Journal of Chemical Physics*, Vol. 97, No. 3, 1992, pp. 1838–1849.

[17] Hedin, A. E., "A Revised Thermospheric Model Based on Mass Spectrometer and Incoherent Scatter Data: MSIS-83," *Journal of Geophysical Research*, Vol. 88, No. A12, 1983, pp. 10170–10188.

[18] Hedin, A. E., "MSIS-86 Thermospheric Model," *Journal of Geophysical Research*, Vol. 92, No. A5, 1987, pp. 4649–4662.

[19] Hedin, A. E., "Extension of the MSIS Thermosphere Model into the Middle and Lower Atmosphere," *Journal of Geophysical Research*, Vol. 96, No. A2, 1991, pp. 1159–1172.

[20] Knecht, D. J., Murad, E., Viereck, R., Pike, C. P., Broadfoot, A. L., Anderson, E. R., Hatfield, D. B., Stone, T. C., and Sandel, B. R., "The Arizona Airglow Experiment as Flown on Four Space Shuttle Missions," *Advances in Space Research*, Vol. 19, No. 4, 1997, pp. 627–630.

[21] Tang, X., *Diatomic, a Spectral Simulation Program for Diatomic Molecules*, http://www.diatomic.com, 2004.

[22] Bird, G. A., *Molecular Gas Dynamics and the Direct Simulation of Gas Glows*, Clarendon, Oxford, England, U.K., 1994.

[23] Lias, S. G., Bartmess, J. E., Liebman, J. F., Holmes, J. L., Levin, R. D., and Mallard, W. G., "Gas-Phase Ion and Neutral Thermochemistry," *Journal of Physical and Chemical Reference Data*, Vol. 17, Supplement 1, 1989, p. 1.

I. Boyd
Associate Editor